A Method To Implement Permeability Anisotropy Associated With Fault Damage Zones in Reservoir Simulation

Pijush Paul, SPE, and **Mark Zoback,** SPE, Stanford University; and **Peter Hennings,** ConocoPhillips

Summary

In this study, we present a method to incorporate the effects of fault damage zones (DZs) in a reservoir-simulation model. Permeability anisotropy associated with fault DZs depends on many factors, including the geometry of the faults in the reservoir and the associated dimension and density of fractures in the DZs. To model permeability anisotropy caused by fault DZs, we start by using geomechanically constrained discrete fracture models of DZs. Then, we use the orientation and size of the faults with reference to the grid axes to incorporate the effect of permeability anisotropy in the simulation grid. In this case study, in which faults are formed in an extensional regime, DZs show increased permeability along the strike of the fault and in the vertical direction, but there is no significant change in the permeability perpendicular to the faults. Inclusion of DZs in the simulation model shows significant improvement in the history matching in comparison to a base reservoir-simulation model with no DZs. Further, we analyze the uncertainty of the DZ modeling in the reservoir simulation by simulating multiple equiprobable models.

Introduction

Fluid flow through secondary fractures associated with DZs adjacent to large faults can be significant in many reservoirs. These effects can be represented in reservoir simulation by adding them either in the fine-scale geological model or in a coarse-scale reservoir-simulation model. DZs may contain many secondary fractures, so including each one as a discrete feature in the simulation model is limited by the computational power and time of the reservoir simulator (Durlofsky 2003; Geiger et al. 2009; Lim et al. 2009). However, there has been considerable progress made in upscaling the flow effects of small-scale geological heterogeneities (Corbett et al. 1992; Ringrose et al. 1993; Pickup et al. 2000a, 2000b; Flodin et al. 2001; Jourde et al. 2002; Durlofsky 2003; Ahmadov et al. 2007; Gong et al. 2008). These upscaling techniques are successful at maintaining the average flow behavior of the reservoir in some scenarios, but discrete-fracture techniques may be required for some water-injection problems.

Fractured porous media are typically simulated using dual-porosity models, but these models are not suited for reservoirs with only a few fractures or localized fracture zones that dominate flow. Ideally, faults are defined as discrete features in an upscaled model, but to maintain their complex geometries, special discretization scheme and multipoint flux approximation adjacent to the faults have to be used (Verma and Aziz 1997; Rodriguez et al. 2004). Also, upscaling and history matching using a number of geological scenarios with fault-DZ fractures can be a lengthy process. An alternative that includes the effects of fractures associated with the faults is a multilaminate model (Pande 1980; Koutsabeloulis et al. 1994), in which first a base upscaled model with reservoir-scale faults and stratigraphical heterogeneities is constructed. Then, different scenarios of the effects of the localized fractures are included on the base model. In this technique, fractures are treated as an effective medium, spatially changing the base-model properties in localized areas. Various techniques may be used to define localized, fine-scale heterogeneities on an upscaled grid such as local grid refinement (LGR) (Ciment and Sweet 1973; Pedrosa and Aziz 1986; Nacul 1991) and a windowing technique (Mlacnik and Heinemann 2003). However, the effectiveness of these techniques depends on the type of upscaled grid, the type and scale of localized heterogeneity, and the ability of the reservoir simulator to handle these treatments.

In this paper, we describe a workflow to incorporate geomechanically constrained DZs in reservoir simulation using a multilaminate technique. Paul et al. (2009) describe a method to model geomechanically constrained fault DZs. Fault DZs (secondary faults and fractures associated with the main fault) are formed during the propagation of a rupture along a main fault (Madariaga 1976; Freund 1979). Stress concentration along the propagation path can be used to model the width and nature of a DZ associated with the reservoir-scale faults. In this case study, we use the DZ descriptions from Paul et al. (2009) and present a discrete-fracture-modeling experiment to show the effects of the DZ an the permeability of an upscaled block. Then, we incorporate the effect of the DZs in the reservoir-simulation model, which is a nonorthogonal grid with corner-point geometries. Adjacent to the fault, gridblocks are truncated to maintain the actual shape of the faults. We discuss a workflow to include permeability anisotropy in the fault-adjacent gridblocks of the base simulation model and to quantify the effects using history matching of the production and injection data.

Field-Scale Permeability Anisotropy and Project Motivation

The chosen study area (CS field) is located in the Timor gap between Australia and Indonesia. **Fig. 1** shows the production, injection and exploration wells of the field. Interference and tracer tests between injection and production wells of the studied field show enhanced flow along the reservoir-scale faults. Larger east/west-trending faults indicate a relatively high connectivity parallel to these faults in comparison to the north/south-trending faults. Well CSP3 shows a clear indication of pressure communication with Wells CSP1 (approximately 2.5 km), CSP2 (approximately 1.5 km), CSP4 (approximately 3.5 km), and injectors (>6 km) within 24 hours. Well CSP4 also sees pressure support from injectors (approximately 4.5 km), but the response is delayed relative to Well CSP3 even though the injectors are closer, indicating a lower permeability from injectors to Well CSP4 when compared with Well CSP3. Well CSP7 shows pressure communication with Well CSP6 (approximately 3 km) after 30 hours and with Well CSP5 (approximately 1.5 km) after 12 hours, a delayed response relative to the responses of Well CSP3. Injector pressure support in Well CSP7 is observed after 48 hours, which is again a delayed response relative to pressure support from injectors to Wells CSP3 and CSP1 to the east. To summarize these observations, the blue lines in **Fig. 1** indicate established hydraulic connectivity among the wells.

Comparing the bottomhole pressure (BHP) and water-production rate (WPR) response from the base simulation model, which has porosity and permeability distributions from classical geostatistical techniques (described later in this paper), shows a poor history match with actual production and injection data from the

Original SPE manuscript received for review 30 September 2009. Revised manuscript received for review 1 October 2010. Paper (SPE 143305) peer approved 11 October 2011.

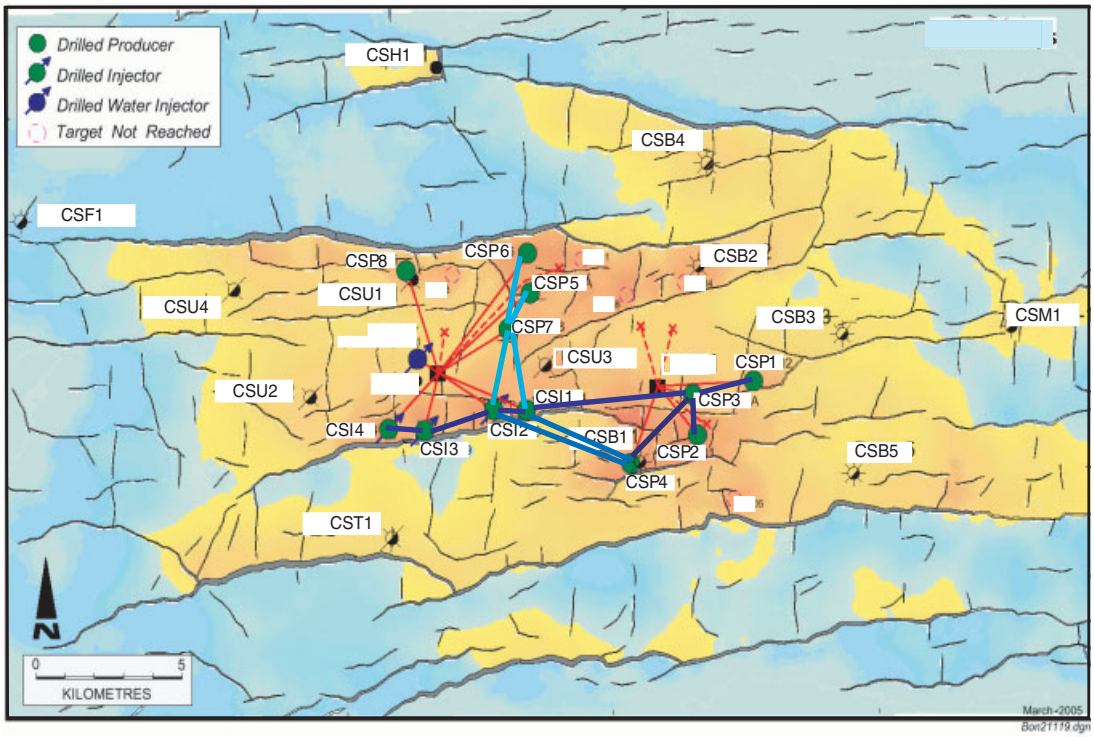

Fig. 1—Map shows the relative locations of injectors (Wells CSI1 through CSI4), producers (Wells CSP1 through CSP8), and exploration wells. Red lines indicate well path. Blue lines in the figure show established pressure contact among wells during interference and tracer tests. The darker blue color represents the paths with relatively shorter well interaction time than those of the lighter colors. Flow along the faults shows enhanced permeability with respect to the average matrix permeability of the reservoir. The background color of the map is the depth of the reservoir (warmer color represents shallower depth).

wells. On the basis of observations from tracer and interference tests, we include the localized enhanced permeability parallel to the reservoir-scale faults, which shows a better history match in comparison with the history match from the base model. The enhanced fault-parallel permeability is hypothesized as an effect of fault DZs. In this paper, we propose a workflow for incorporating the permeability variations because of DZs into the reservoir-simulation model. The conclusions from this study are based on the history matching of production data for approximately 2.5 years from the initial production.

Permeability Anisotropy Caused by a DZ Using Discrete-Fracture-Network (DFN) Modeling

To model the trend and magnitude of the permeability anisotropy caused by fault DZs, we use 2D and 3D discrete-fracture modeling. In this study area, Paul et al. (2009) estimated the width of DZs as approximately 150 m for large reservoir-scale faults and approximately 50 m for smaller faults. A 3D DFN study investigated the relative trend of permeability anisotropy in an average block size of the reservoir-simulation model. Hence, the size of the 3D model was the following: depth of 80 m (average depth of gridblocks), width perpendicular to the fault of 380 m (average width of gridblocks), and length along the fault of 100 m (approximately one-third of the average length of gridblocks). The fractures and faults in the DZ are defined as discrete features using a dynamic rupture technique (Paul et al. 2009) combined with Monte Carlo simulation to incorporate the uncertainty in their locations and geometry. Fracture planes mostly strike subparallel (maximum deviation of approximately 30°) to the fault. Fracture density in the model decreases away from this fault face and becomes zero beyond the limit of the DZ (approximately 60 m). A discrete-fracture model **(Fig. 2)** with approximately 600,000 cells was used for the study. This model has average fracture density of approximately 0.3 fracture/m and 3–4 vertical stack of fractures in the DZ. In the model, the matrix porosity of approximately 13% and permeability k_m of approximately 150 md are based on petrophysical analysis. Fracture aperture was kept at approximately 1 mm, and fracture permeability k_f varies as a multiplier of k_m, which is based on field and laboratory studies (Brown and Bruhn 1998; Luthi and Souhaite 1990). We used a range of multipliers from 10^2 to 10^6 (extreme case) with k_m to define fracture permeability. This multiplier range was used to study the effect of contrast between matrix and fracture permeability in the permeability anisotropy of an average gridblock of the simulation model.

One face of the model perpendicular to the flow is defined as an injector well at 1,500 B/D, and the opposite face is defined as a producer with production at a pressure constraint equivalent to reservoir pressure, 4,000 psi. Models with and without DZs are simulated (Karimi-Fard et al. 2004) until steady state is reached, giving the pressure difference ΔP between injector and producer faces of the model. By comparing the pressure difference (ΔP) between the two cases, we can estimate the change in the effective bulk permeability along the flow owing to the presence of fractures,

$$\frac{k_2^*}{k_1^*} = \frac{\Delta P_1}{\Delta P_2}, \qquad (1)$$

where k_1^* and k_2^* are the equivalent, or upscaled, permeabilities, and ΔP_1 and ΔP_2 represent the pressure difference of steady-state solution along the flow for the models with and without fractures. Repeating the experiment in the three possible principal directions with $k_f = 10^3 \times k_m$, we estimated effective-permeability-change factors of 1.36, 1.39, and 1 in the direction subparallel, vertical, and perpendicular to the fault, respectively. By comparing the simulation results for different permeability-contrast cases, we conclude that the anisotropy effect increases only with increasing contrast between the matrix and fracture permeability.

The 3D modeling demonstrates that the effective permeability in the vertical direction is similar to that of the horizontal direction

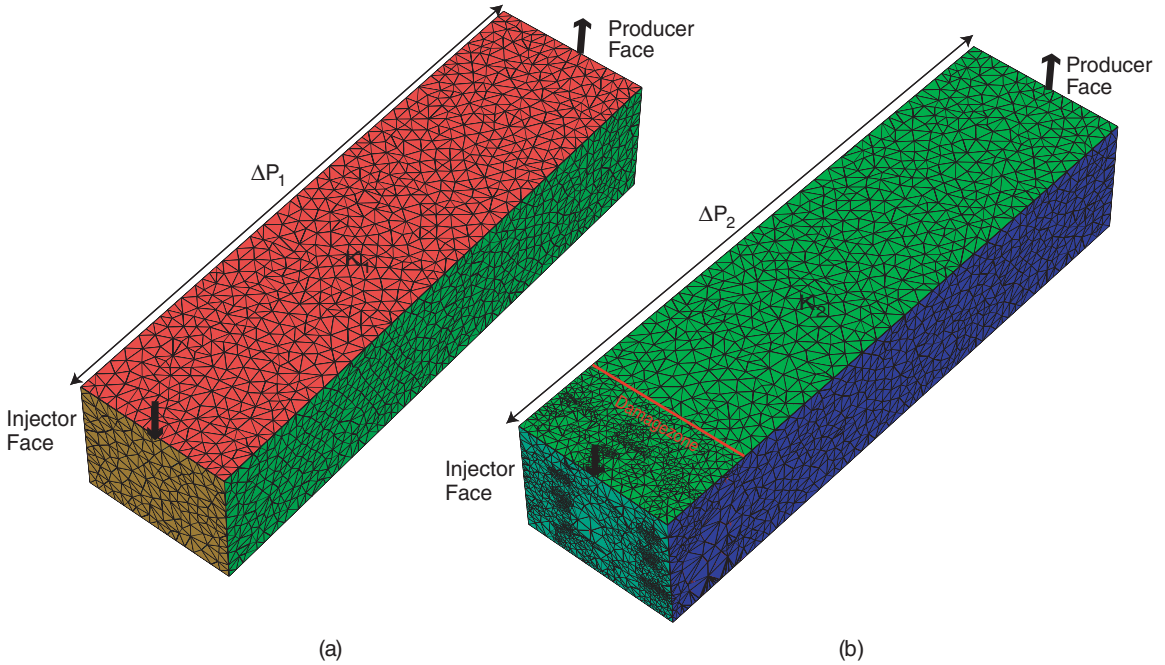

Fig. 2—The fine-scale unstructured grid (a) without a DZ and (b) with discrete fractures and associated matrix blocks of a DZ. (The DZ is represented as very fine grid cells.) In a steady state with similar injection and production constraints, the ratio of pressure difference between the injection and production face gives the change in effective permeability along the flow direction.

parallel to the reservoir-scale faults. Also, effective permeability in two horizontal directions (parallel and perpendicular to the fault) shows some amount of anisotropy. Therefore, we used two horizontal directions in the 2D modeling **(Fig. 3a),** which represented the actual average gridblock size (approximately 360×380 m) of the reservoir-simulation model, allowing us to use higher fracture density with limited computational expense. In Fig. 3b, simulation results with increasing average fracture density in the DZ indicate a linear increase in permeability of the gridblock in the direction parallel to the fault, but there is almost no change in permeability in the direction perpendicular to the fault. For fracture density of approximately 0.3 fracture/m (same as 3D-model fracture density), the permeability parallel to the fault increases by approximately 1.5 times, which is consistent with the 3D-model results. Wellbore-image analysis indicates a fracture density of approximately 2 fractures/m for a DZ width of approximately 60 m (Paul et al. 2009). For this fracture density, we see an approximately sevenfold increase in the fault-parallel permeability of a grid cell. Within the DZ, permeability increase is approximately 40 times the matrix permeability. Similarly, a wider DZ would show a much higher increase in the cell permeability parallel to the fault. To define the uncertainty owing to geometry (length, orientation, and intersections) of the fractures in the DZ, we repeat the 2D experiments for five equiprobable models with the same fracture density and DZ width for the models. Fig. 3b shows the uncertainty range of permeability multiplier (spread of red triangles) for a fracture density of approximately 1.3 fractures/m. Uncertainty range is approximately 0.5 for fault-parallel multiplier, which indicates the uncertainty of the fracture network in the DZ. However, an uncertainty range of approximately zero for fault-perpendicular multiplier confirms a nonfactor change in permeability in the direction perpendicular to the fault.

3D Geocellular Model

The chosen study area has a number of large reservoir-scale faults striking in the east/west (E/W) direction and several small-scale faults with a north/south (N/S) orientation. These faults are formed in an extensional environment. The average throws for E/W and N/S faults are approximately 300 and 50 m, respectively. Reservoir layers are from a fluvial-deltaic-dominated depositional environment and they comprise medium- to coarse-grained sandstone to very-fine- to fine-grained shale (Paul et al. 2009).

The geocellular model of the reservoir is a nonorthogonal grid with 300×160×265 cells in the *x*-, *y*-, and *z*-directions, respectively. It has 183 modeled faults and 265 layers. The reservoir is a broad E/W-trending horst with closure at 2930 m subsea to the gas/water contact at 3108 m subsea. Fluid samples collected from drillstem tests (DSTs) indicate that the reservoir acts as a single compartment with common gas/water contact. Matrix porosity and permeability in the model are defined on the basis of the reservoir quality, which is guided by grain size, sorting, and lithofacies. Porosity in the model varies from 2 to 20%, with an average value of 8.6%. Horizontal and vertical permeability in the model lie in the range of 0.001–900 and 0.001–400 md with average values of approximately 150 and 60 md, respectively. Porosity and permeability distributions are modeled using the paleocurrent transport models from seismic and well data.

Base Simulation Model

The geocellular model is upscaled to a simulation model using an irregular nonorthogonal grid with a grid size of 80×46×45 cells in the *x*-, *y*-, and *z*-directions, respectively. The 45 layers in the *z*-direction represent the 19 stratigraphic units or 265 layers of the geocellular model. Average layer thickness varies from 3 to 20 m. The field is divided into six parts **(Fig. 4)** with different upscaling ratios to honor the heterogeneity of the reservoir. We can see in Fig. 4 that in the main gas-bearing section, the simulation model is relatively fine with respect to other parts of the reservoir.

Porosity is upscaled using arithmetic averaging. Horizontal permeability (k_h) for fluvial layers is upscaled using a hybrid arithmetic-harmonic algorithm (Rasaei and Sahimi 2009), while marine layers are upscaled using a hybrid harmonic-arithmetic algorithm (Aarnes et al. 2009) to capture the lateral reservoir heterogeneity. Vertical permeability (k_v) is upscaled using harmonic-arithmetic averaging. In the gridblocks with shale layers having $k_v < 0.1$ md, k_v is set to zero to define these layers as a barrier to flow in the vertical direction. Water saturation is upscaled using a porosity-weighted averaging algorithm. **Figs. 5a and 5b** illustrate the porosity and horizontal permeability distribution of one reservoir layer (Layer 18) of the base simulation model, respectively. The porosity and

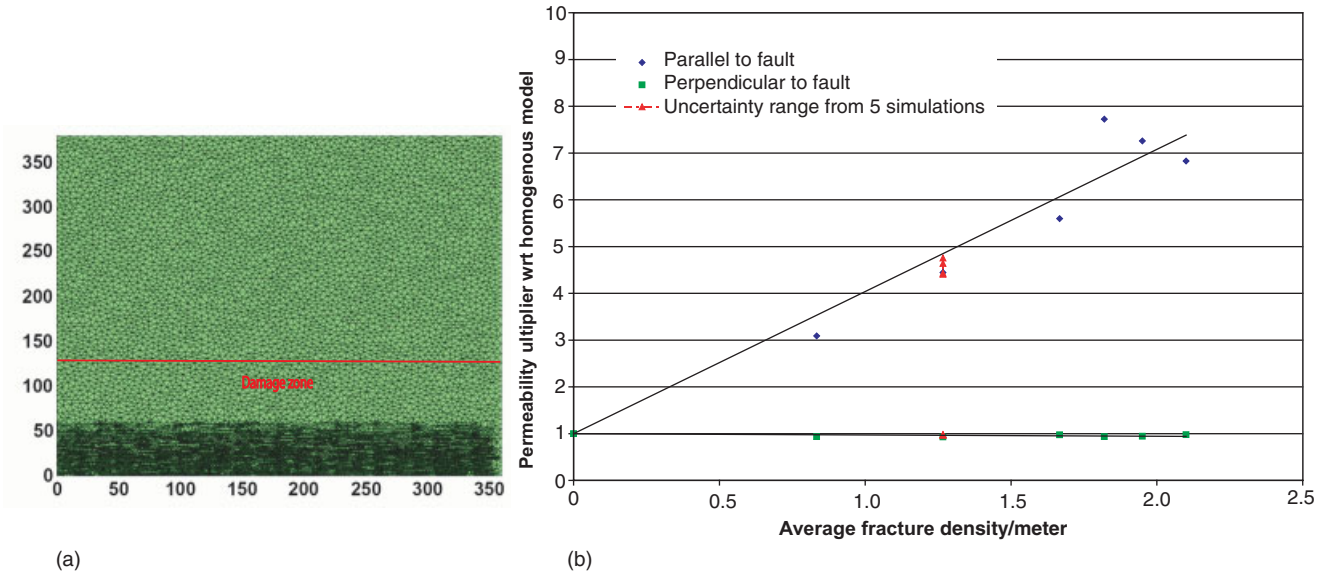

Fig. 3—(a) A 2D unstructured grid with a DZ width of approximately 60 m and an average fracture density of approximately 0.8 fractures/m. Fractures are represented as dark lines in the DZ, and they have associated matrix blocks. (b) Permeability parallel to the fault increases linearly with the increase of fracture density in the DZ with a width of approximately 60 m, but there is no change in permeability in the direction perpendicular to the fault. Red points indicate the uncertainty range of the permeability multiplier from five simulations for a fracture density of approximately 1.3 fracture/m in directions parallel and perpendicular to the fault.

permeability distributions are biased toward well data, which are treated with higher importance during paleocurrent modeling.

The simulation model has 162 faults. Adjacent to the faults, grid cells are highly nonorthogonal and have irregular shapes (Fig. 4). Because faults are not aligned to the grid axes, cells are truncated to honor the actual orientation and shape of the faults. Because of these complexities, a reservoir simulator with a two-point flux calculation can perform only an approximate calculation for this part of the grid.

Initial Conditions and Fluid Properties for Reservoir Simulation. Initial formation pressure obtained from downhole testers (modular formation dynamic tester and repeat formation tester) shows initial reservoir pressure of approximately 4,486 psi at

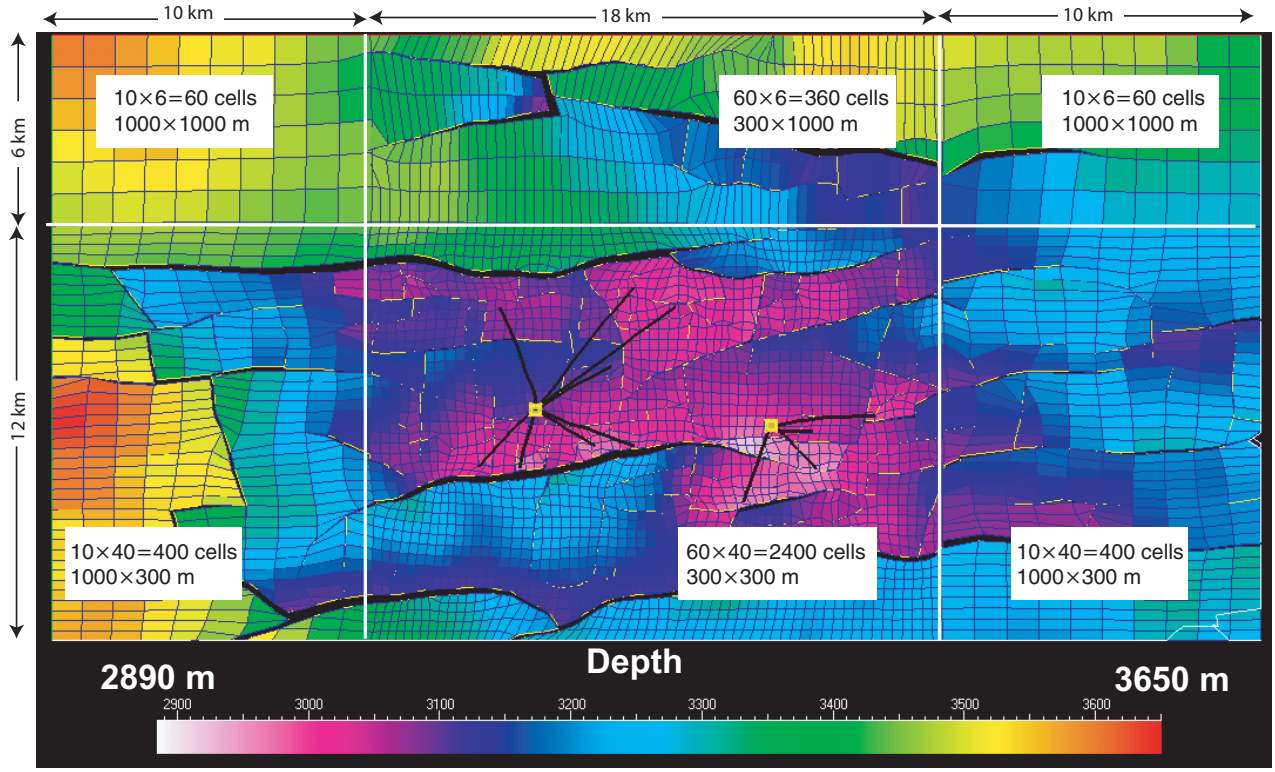

Fig. 4—Depth of Layer 18 of the upscaled model. Main reservoir is located at the shallowest areas (indicated by pink color on the map). Black lines with yellow head (platforms) indicate injector and producing wells. In the reservoir part of the upscaled grid, the number of cells is kept relatively high to honor the heterogeneity.

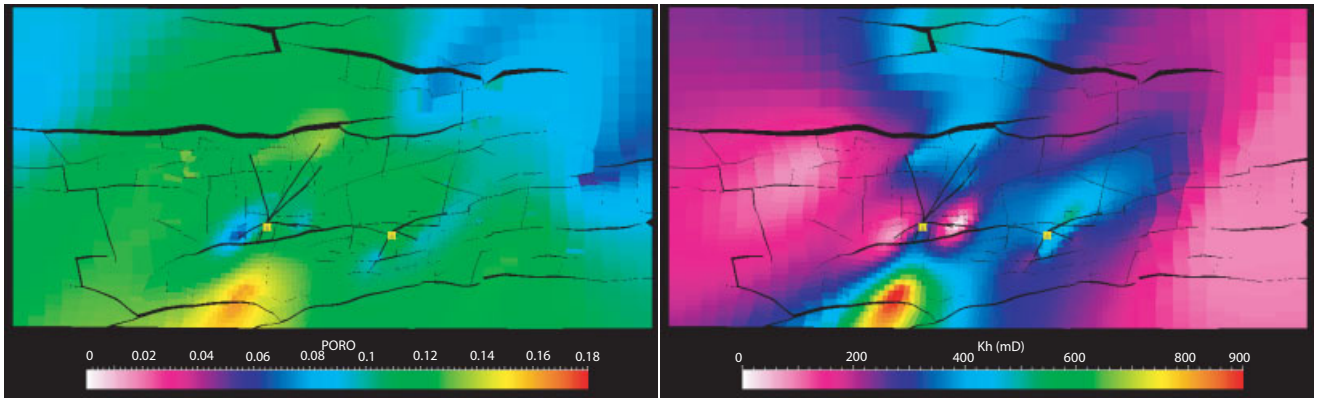

(a) (b)

Fig. 5—(a) Porosity and (b) horizontal permeability (k_h) of the main reservoir section (Layer 18) of the upscaled model. Average porosity is 13%, and k_h varies from 1 to 900 md in the layer.

the gas/water contact at approximately 3109 m subsea, which is common in all the appraisal wells. Pressure-gradient analysis with the tests shows a normal water gradient of 1.37 psi/m and a gas gradient of 0.35 psi/m. Compressibility of the rock matrix is obtained by uniaxial compressive testing on the core samples from exploration Well CSB2. Testing suggests a very stiff and strong reservoir rock, with a range of compressibility from 1.2×10^{-6} psi^{-1} to 3.8×10^{-6} psi^{-1}.

Initial water saturation (S_{wi}) is defined as a function of porosity, permeability, and height above the free-water level (to include the effect of capillary pressure in transition zones), and is calibrated using core measurements and log data. **Fig. 6** shows initial water-saturation distribution in the reservoir section, indicating an average value of S_{wi} of approximately 10%. Residual gas saturation (S_{gr}) is obtained from core measurements using a brine immersion/imbibition technique, which gives a range of 20–30% with an average value of 26.6%.

The relative permeability of the water at residual gas saturation is measured on core samples from the appraisal wells. The average relative permeability is 0.24 at residual gas saturation. **Figs. 7a and 7b** show the oil/water and oil/gas relative permeability curves used for reservoir simulation, respectively.

The simulation model of the CS field is a compositional model with eight hydrocarbon pseudocomponents (C_1/N_2, C_2/CO_2, C_3, C_4, C_5/C_6, C_7–C_{11}, C_{12}–C_{19}, and C_{20+}) and three fluid phases. The properties of hydrocarbon fluids within the reservoir are defined using the Peng-Robinson equation of state (Søriede and Whitson 1992). Properties of the water phase are measured from the samples collected during the DST in Well CSU2. Hydrocarbon fluid in the CS-field reservoir is a retrograde gas/condensate with a measured dewpoint of 4,320 psia, which is lower than initial reservoir pressure of 4,486 psia. Gas-formation-volume factor is 0.7921 RB/Mscf, and viscosity is 0.0304 cp. Samples collected during DSTs in Wells CSB1, CSB2, CSU1, and CSU2 show similar and uniform hydrocarbon-fluid composition across the field. Despite the similarities in the composition condensate, yield in the wells located in the east of the field varies between 63–65 bbl/MMscf, whereas wells in the west side show a value between 69–70 bbl/MMscf. As a result, these zones are defined as two separate initial-composition regions during the simulation.

Constant-volume experiments indicate that the maximum liquid-phase volume is approximately 2.4% of total saturation volume at 1,300 psi, which shows that most of the hydrocarbon volume is mobile and recoverable from the reservoir. Production in the field

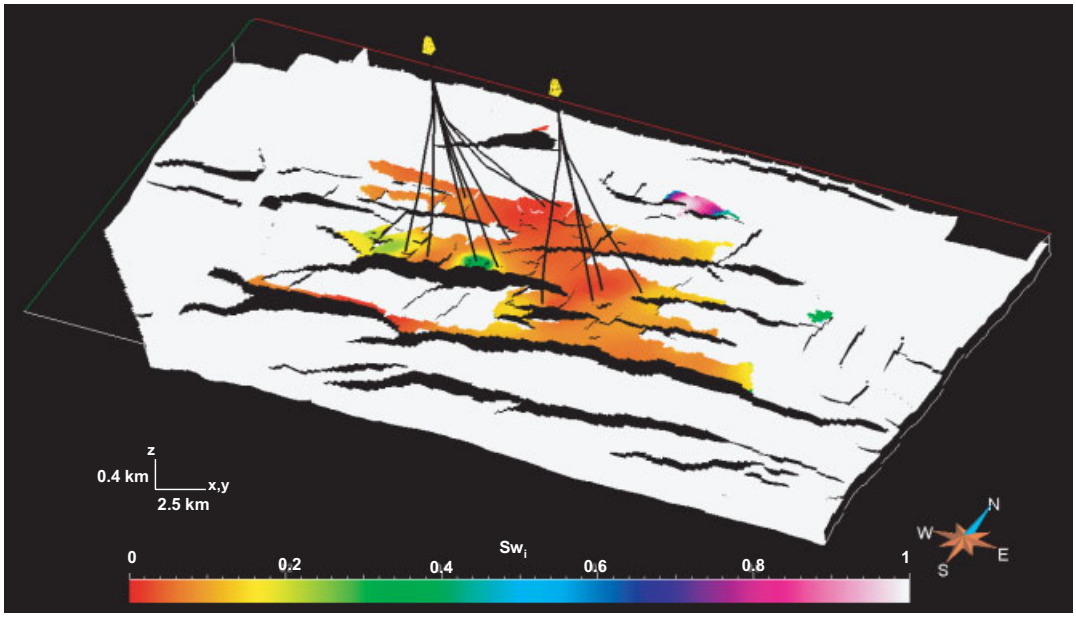

Fig. 6—Initial water saturation at reservoir depth of the CS field. Average initial water saturation is approximately 10% in the reservoir section.

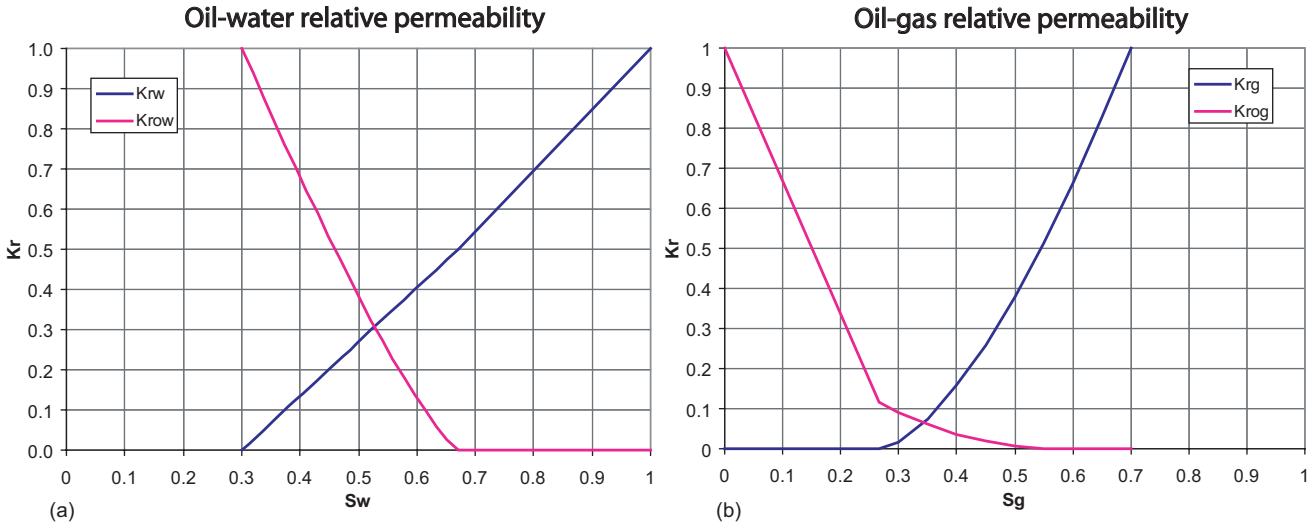

Fig. 7—(a) Oil/water and (b) oil/gas relative permeability used during the simulation. Residual water and gas saturations are approximately 30 and 26%, respectively. Initial water saturation in the reservoir is less than 30%, indicating that water from the reservoir will not flow during primary production.

is constrained by hydrocarbon-production rate. The reservoir is normally pressured by the aquifer, so the latter has a significant impact on overall recovery. In the model, the aquifer volume is considered to be at least 100 times the pore volume.

The response from the base simulation model shows a poor match for injection and production wells with actual field observations. Thus, we improve the model by adding the effect of DZs. In the next section, we discuss how to implement the effects of DZs in the gridblocks adjacent to the faults, honoring the aforementioned complexities.

Implementation of the DZ in the Upscaled Grid

The extent of DZs was estimated using a dynamic rupture-modeling technique (Paul et al. 2009). This technique uses rupture propagation along a fault plane to model the width and nature of DZs associated with faults. In the study area, faults were mostly formed in an extensional stress environment. As indicated by 2D and 3D DFN modeling, a DZ increases the permeability in vertical and fault-parallel directions, but causes no permeability change in the fault-perpendicular direction. **Fig. 8** shows a schematic of the change in cell permeability caused by a DZ. Fault-parallel permeability k_1 in the DZ is many times higher than isotropic base permeability k_h. Depending on the orientation of the fault, a DZ introduces permeability anisotropy in the associated grid cells, which can be difficult to define if these grid cells are nonorthogonal and larger than the DZs. Ideally a full permeability tensor, multipoint flux approximation, and/or LGR are used in the fault-adjacent gridblock to implement the DZ effect in the simulation model. However, these modifications may make the simulation slow because of convergence issues. In addition, there are limitations with the simulator in handling any of these modifications in the simulation model, so we approximate the anisotropy effect by changing permeabilities of the fault-adjacent gridblocks in the *x*-, *y*-, and *z*-direction. Also, we assume that the porosity change is negligible because fracture volume in the DZ is small in comparison to the total pore volume of a gridblock. Following are the three effects of DZ that we incorporate in a simulation grid:

(1) Effect of size of the DZ: normalized DZ width (NDZW)

(2) Effect of anisotropy in the DZ: normalized permeability factors (NPFs) in *x*-, *y*-, and *z*- direction

(3) Effect of fracture density in the DZ: fracture density constant *m*

We transform these three effects into multiplier functions that can be used to estimate permeability changes in the base model at fault-adjacent grid cells. Eqs. 2a, 2b, and 2c define the multiplier

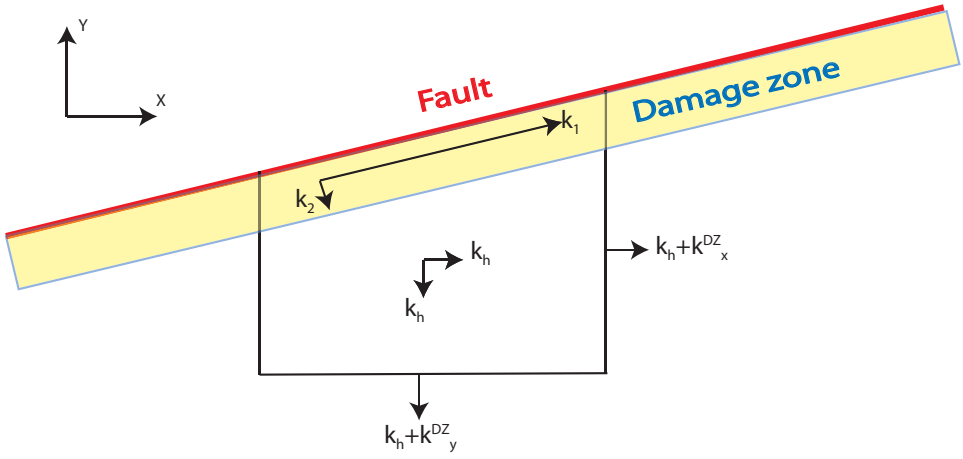

Fig. 8—Anisotropy in a generalized grid cell adjacent to a fault in the reservoir-simulation model. Fault-parallel permeability k_1 is an order of magnitude higher than grid-cell permeability k_h but fault-perpendicular permeability k_2 is approximately equal to k_h, which gives a complex anisotropic condition for a nonorthogonal grid cell truncated on the fault face.

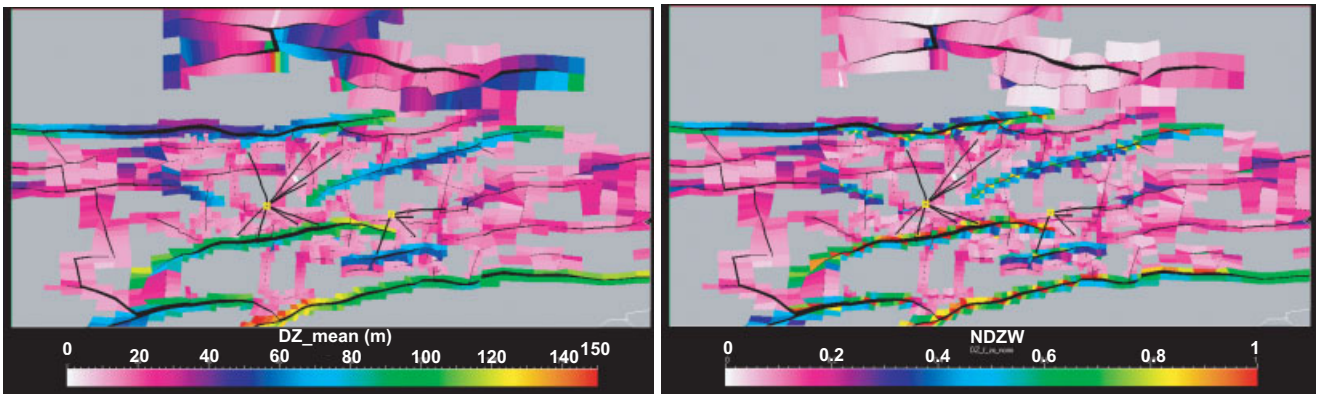

(a) (b)

Fig. 9—(a) DZ mean on Layer 18 of the upscaled grid. Mean is estimated from 100 equiprobable simulations of the DZ estimation using the dynamic rupture-propagation technique (Paul et al. 2009). (b) Estimated values of NDZW on Layer 18 of the upscaled grid. Smaller grid cells adjacent to same fault show high NDZW value.

functions in the *x*-, *y*-, and *z*-direction, and are called as absolute-permeability multipliers (APMs). In the presence of a DZ, normalized width and normalized permeability factors in the *x*-, *y*-, and *z*-direction guide the value of multipliers. Fracture-density constant *m* scales the variability of fracture density in the DZs associated with faults of different geometries. For a grid cell without a DZ, (NDZW × NPF ×m) equals zero, which converts these multipliers (APMs) to 1. In the following sections, we describe how to estimate the variables (*NDZW, NPF,* and *m*) for the fault-adjacent grid cells.

$$APM_x = 1 + (NDZW)(NPF_x)(m), \quad \ldots\ldots\ldots\ldots\ldots\ldots (2a)$$

$$APM_y = 1 + (NDZW)(NPF_y)(m), \quad \ldots\ldots\ldots\ldots\ldots\ldots (2b)$$

$$APM_z = 1 + (NDZW)(NPF_z)(m). \quad \ldots\ldots\ldots\ldots\ldots\ldots (2c)$$

Effect of Size of the DZ (NDZW). Paul et al. (2009) shows that the absolute widths of the DZ are related to the size of the faults, location of the rupture event, and material properties. For this study area, DZ widths were estimated by dynamic rupture technique. The mean DZ width (DZ_mean) of 100 equiprobable simulations ranges approximately from approximately 40 to 50 m for small faults and from approximately 90 to 120 m for large faults. The standard deviation of 100 simulations is approximately 15 m for smaller faults and approximately 60 m for larger faults. The effect of a DZ depends on the relative size of the DZ width and the block size. We define the DZ in a normalized relative scale (0 to 1) for the whole grid and call it the NDZW. DZs run subparallel to reservoir-scale faults, but their width extends normal to the plane of the fault. To normalize the DZ width we divide actual DZ width by the effective-grid-cell width normal to the fault. Effective width in the *x*- and *y*-directions can be defined as bulk cell volume (CV) divided by cross-section area ($dz \times dx$) and ($dz \times dy$), respectively. In this study, *x*- and *y*-directions are aligned with E/W and N/S directions. Eqs. 3a and 3b show NDZW for the faults trending in E/W and N/S directions, respectively. **Fig. 9b** shows the NDZW values for Layer 18 of the simulation grid. We can see that smaller cells associated with the same faults have higher NDZW. Also, cells associated with larger faults have higher NDZW because they have wider DZs. For an example, the fault in the southern most part of the field in Fig. 9a has DZ_mean of approximately 100 m (greenish area). In the same region (Fig. 9b), NDZW varies from approximately 1(red) to 0.6 (green) for small to large cells, respectively.

$$NDZW_{EW} = \frac{(DZ\_\text{mean})(dx)(dz)}{CV}, \quad \ldots\ldots\ldots\ldots\ldots\ldots (3a)$$

$$NDZW_{NS} = \frac{(DZ\_\text{mean})(dy)(dz)}{CV}. \quad \ldots\ldots\ldots\ldots\ldots\ldots (3b)$$

Effect of Anisotropy Because of the DZ (NPF). The DFN study of the DZs shows that the maximum permeability enhancement is along the fault strike and in the vertical direction. However, depending on the relative orientation of the fault with respect to the grid axes, the permeability enhancements are distributed in *x*-, *y*-, and *z*-direction. The horizontal (*x* and *y*) and vertical (*z*) components of the permeability multiplier are related to the strike and dip of the fault, respectively. We approximate the anisotropy effect using the magnitude of the dot product of the full permeability tensor and the normal vector of the grid faces for the DZ. This is a reasonable approach because the permeability-anisotropy effect is relatively high in the direction parallel to faults compared to perpendicular to faults, and most of the faults are aligned either to E/W (*x*-direction) or to N/S (*y*-direction). In the Uncertainty in the Simulation Response section, we discuss uncertainty related to the different anisotropy-distribution techniques, which can be used in more general scenarios in which faults and grid axes are not parallel. Eq. 4 represents the anisotropy coefficients in the *x*-, *y*-, and *z*-direction, and in this study we refer to these components as an NPF. **Figs. 10a through 10c** illustrate the NPF values for Layer 18 on the simulator grids in the *x*-, *y*-, and *z*-direction, respectively. We can see that faults aligned in the EW direction have high NPF in the *x*-direction while the faults aligned in the N/S direction have a higher *y*-component. Also, the N/S-trending faults have a higher *z*-component because they have a comparatively higher dip angle than the E/W faults.

$$NPF_x = |\sin(\text{strike})|, \quad \ldots\ldots\ldots\ldots\ldots\ldots (4a)$$

$$NPF_y = |\cos(\text{strike})|, \quad \ldots\ldots\ldots\ldots\ldots\ldots (4b)$$

$$NPF_z = |\sin(\text{dip})|. \quad \ldots\ldots\ldots\ldots\ldots\ldots (4c)$$

Effect of Fracture Density in the DZ. Fracture density of the DZ can be estimated using well-scale information such as wellbore images. Paul et al. (2009) shows that fracture density in the study area gradually increases with proximity to the reservoir-scale faults. Also, dynamic rupture modeling indicates that fracture density in the DZ is directly proportional to the energy released during

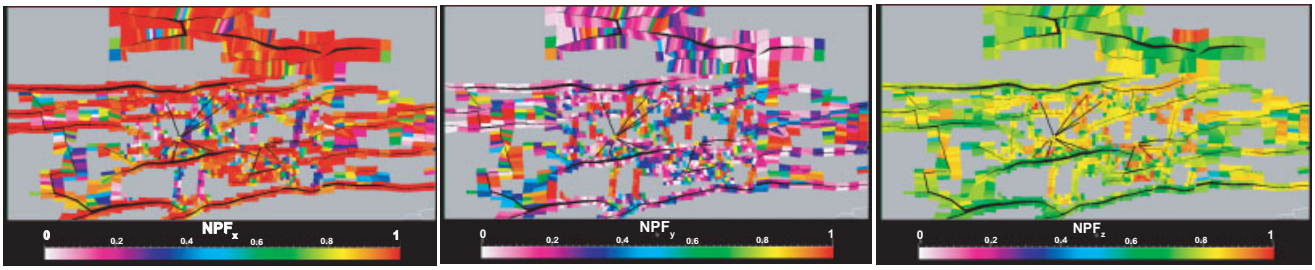

(a) (b) (c)

Fig. 10—Estimated values of the NPF in (a) *x*-direction, (b) *y*-direction, and (c) *z*-direction on Layer 18 of the upscaled grid. It shows relatively high connectivity in the *x*-direction along the large reservoir-scale faults trending in the E/W direction and relatively high *y*-direction and vertical connectivity adjacent to the N/S-trending faults.

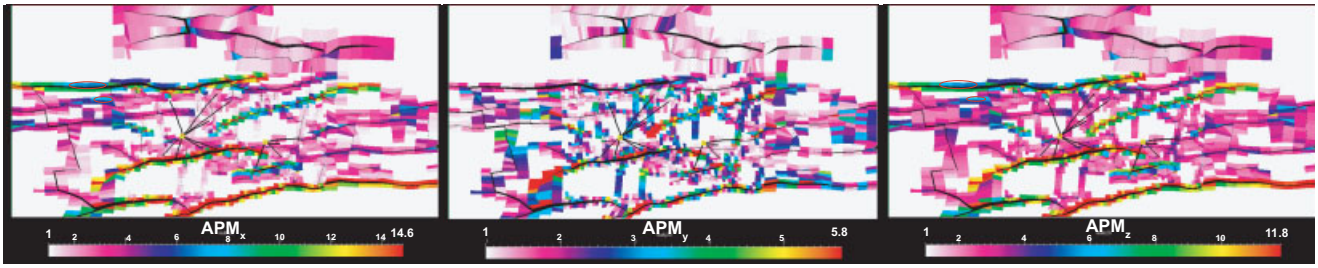

(a) (b) (c)

Fig. 11—APM in (a) *x*-, (b) *y*-, and (c) *z*-direction on Layer 18 shows multiplier values up to approximately 15 in *x*-direction and approximately 12 in *z*-direction adjacent to the E/W-trending faults. In *y*-direction, permeability multipliers are of relatively low values.

the rupture event. Also, DZ width is proportional to the energy released. Hence, fracture density is proportional to the width or size of the DZ. We used a proportionality constant m in the multiplier functions to define the variability of fracture density in the simulation model. The value of m is constant for a model, and it scales the effect of fracture density by relative width of fault DZs. In this study, the value of m is determined using iterative history matching. This can also be determined using fracture density from wellbore images and DFN modeling, but it can be computationally expensive to do this for all the faults in a reservoir.

Figs. 11a through 11c show the APM values in the x-, y-, and z-direction, respectively, using m=20 for Layer 18 on the simulation grids. Permeability enhancement of the fault DZs using m=20 in the multiplier functions (Eq. 2) gives the best history match. The permeability multipliers (APMs) in the model needed for the history match (for a gridblock size of approximately 360×380 m, with DZ width of approximately 60 m and fracture density of approximately 2 fractures/m, red circled blocks) in the vertical direction and parallel to the faults are approximately 6–7. This value is consistent with the permeability multiplier obtained from the DFN modeling for the gridblock of the same size with similar DZ width and fracture density (Fig. 3). The consistency of these independent techniques validates the DZ modeling and implementation techniques in this study and suggests that m=20 indicates a fracture density of approximately 2 fractures/m for the cell size of approximately 360×380 m and DZ width of approximately 60 m. That means the permeability-multiplier relationship for DZs from DFN modeling (lines in Fig. 3b) can be represented by Eq. 2. The coefficients (*NDZW, NPF,* and m) can be obtained from a gridblock (with similar size and DZ width similar to those of the DFN model) of the history-matched simulation model.

Figs. 12a through 12c show the modified permeability for the history-matched model in the x-, y-, and z-direction, respectively. The x-direction (E/W) permeability ranges from 400 to 3,200 md in the gridblocks adjacent to the faults. Higher values are associated with the larger faults, which are the major paths to give a

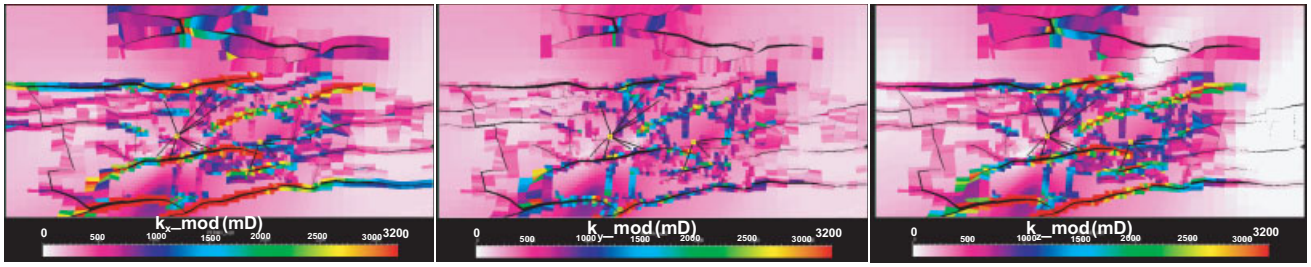

(a) (b) (c)

Fig. 12—Modified permeability in the (a) *x*-, (b) *y*-, and (c) *z*-direction on Layer 18 of the simulation model. Large E/W-trending faults show high permeability anisotropy along the fault in *x*- and *z*-direction. Anisotropy in *y*-direction is relatively low because of smaller faults in the N/S direction.

preferential flow in the E/W direction. This is also observed in interference and tracer tests. The average value for the modified k_y is much lower than k_x values, which is consistent with the low connectivity in the N/S direction indicated by the tests. Some of the high k_y values are associated with the inclined part of the E/W-trending fault, giving a high *y*-component. The k_z values are relatively higher (1,000–3,000 md) in the blocks associated with the larger faults, which may explain observations of good pressure support and some of the water production from the aquifer. However, interbedded shale layers with very low permeabilities are still the barrier for overall vertical flow.

History Matching

In this section, we compare the history matching of the base reservoir-simulation model with the history matching of the reservoir-simulation model with the DZs. Fig. 1 shows the locations of production (CSP1 through CSP8) and injection (CSI1 through CSI4) wells in the CS field. The CS field is a condensate reservoir. Production and injection from the field are constrained by gas-production and -injection rates, respectively. BHP and WPR from model response and field observation are compared quantitatively to conduct history matching. **Table 1** illustrates the listing of quantitative history matching for cases with *m* value of (10, 20, and 30). All three cases show improvement from the base case. For the *m*=20 case, both BHP and WPR are improved from the cases with *m* value of 10 of 30. Blank boxes in the table indicate unavailability of the field data. Also, in some wells, field data (magenta curve in **Figs. 13 and 14**) are available only for a limited production/injection period.

Reservoir Pressure. In the CS field, reservoir pressure is supported by both aquifer and injected gas, so understanding fluid communication in both vertical and horizontal directions is important for assessing reservoir production behavior. In the base simulation model, vertical communication is controlled by vertical permeability and the juxtaposition of faults, and the horizontal communication is controlled by spatial lateral reservoir heterogeneity. Figs. 13a and 13b, respectively, show that injector Well CSI3 simulates higher BHP than observed and producer Well CSP3 simulates lower BHP than observed, which indicates a lack of pressure communication or lower permeability in the base model. Permeability anisotropy caused by DZs supports both horizontal and vertical communication. After including the DZ in the base model, we observe a significant improvement in the history matching of the BHP for both Wells CSI3 and CSP3 (Figs. 13a and 13b, respectively).

In general, for injection wells, the base model overestimates the BHP. A simulation model with DZs, which has higher permeability in the E/W and vertical directions along the larger faults, gives a better history match. All of the production wells located to the east of the injectors and within the major DZ show significant improvement in BHP match with the DZs in the simulation model. Well CSP1, which is located at the flank of the structure (Fig. 1), shows relatively poor history match of BHP after 6 months of production. Aquifer effect is visible even in an earlier period of the production, which is indicated by a sharp decline in BHP. Producers located north of the injectors show an improved history matching with DZs in the model, but the effect was not as significant because DZs for N/S-striking faults are relatively smaller than those for E/W-striking faults.

Water Production. In this field, the initial water saturation in the reservoir section is 0–30%, and most of this is residual water. Detailed relative permeability experiments are not available for this field, so there may be some degree of uncertainty in the residual water saturation and water flow. The initial field condensate water-to-gas ratio was approximately 2.33 bbl/MMcf of raw gas produced. Thus, the main source of free-water production in the large scale is the aquifer below the main reservoir. Two possible ways by which water can encroach on the wells in the early period of production are perforations very close to the water/gas contact and localized heterogeneities such as faults connecting the aquifer to wells. Fig. 14b shows better water-production-rate matching for Well CSP8 from the DZ model. In Fig. 14a, we see that the DZ model shows a better match for cumulative water production than the base model.

In general, for the wells located north of the injector, the DZ simulation model has improved the history matching for the water-production rate. In Wells CSP7, CSP5, and CSP6, water production is relatively low, and both the base model and DZ model show good history matching. Most of the wells located in the east side of the structure have relatively low water production and show a good history match from both models. Well CSP3 started producing water at approximately 1,900 B/D after 1 year of production. The cause was determined to be a perforation in this well that is very close to the oil/water contact. Water breakthrough started once the reservoir was slightly depleted. The reduced cumulative water production with the DZ model can be explained as an increased gravity effect or less coning caused by increased vertical permeability.

TABLE 1—QUANTITATIVE HISTORY MATCHING WITH BHP AND WATER PRODUCTION RATE (WPR) FOR CASES WITH *m* VALUES OF 10, 20, AND 30*

	m=10		*m*=20		*m*=30	
Wells**	BHP (% avg. error)	WPR (% avg. error)	BHP (% avg. error)	WPR (% avg. error)	BHP (% avg. error)	WPR (% avg. error)
CSI1						
CSI2	9		0.6		8.5	
CSI3	3		0.2		3.2	
CSI4						
CSP1	16.5	12.6	3.1	11.4	15.3	13.2
CSP2		31.1		23.4		22.3
CSP3	9.4	9.6	0.6	9.1	9.5	13.6
CSP4	11.5	4.5	0.8	3.7	8.3	3.9
CSP5		8.1		7.5		7.6
CSP6		28.1		27.4		25.3
CSP7	21	4.2	1.8	1.9	17	2.5
CSP8		14.2		7.3		17.5

* Errors are shown in absolute average percentage between observed and simulated values at well locations. Blank spaces indicate unavailability of field data.

** I = Injector; P = Producer

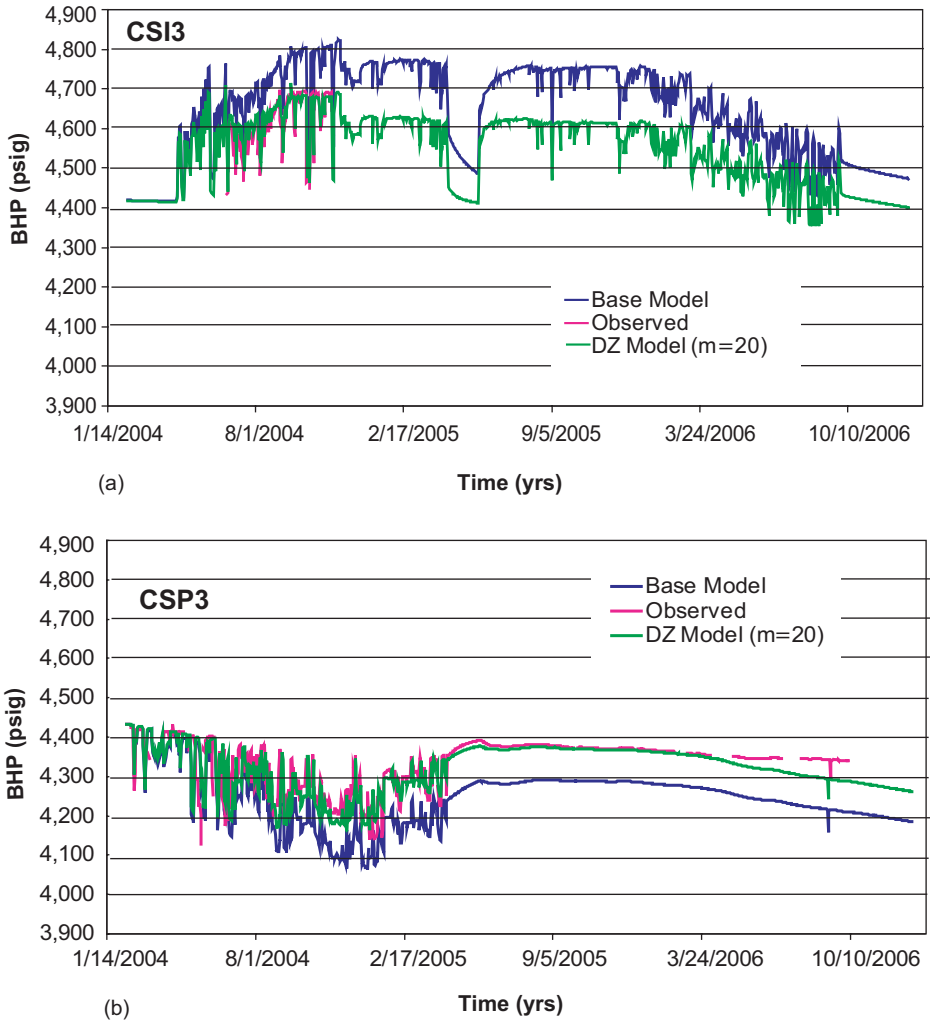

Fig. 13—Comparison of observed BHP (magenta) and simulated BHP from the base model (blue) and the DZ model (green) for (a) injection Well CSI3 and (b) production Well CSP3. The DZ model shows a significant improvement in the history matching in all the wells (Paul et al. 2009).

From the preceding analysis, we can conclude that the response from the DZ model matches better with the observed value than the base model. Thus, the DZ model has definitely improved the base simulation model by including permeability changes because of DZs, which guides the pressure distribution and fluid flow in the reservoir. However, we can see that the water-production match is still not perfect. The possible reasons include the uncertainty in relative permeability of the water, localized heterogeneities that are acting as conductive paths, and the uncertainty in the size of the aquifer.

Uncertainty in the Simulation Response

History matching of BHP and water production shows that the simulation model with DZs gives a better match when compared with the base simulation model. In the following subsections, we include an analysis to capture the uncertainty trends related to the fault-DZ modeling in the simulation model. These uncertainties may come from the width and fracture density of the DZ, and from the method to model the anisotropy because of DZs in the simulation model.

Uncertainty Owing to DZ Modeling. To capture the uncertainty caused by DZ width in the simulation response, we simulate 20 equally likely DZ models. These equiprobable DZ models are created by the dynamic rupture technique considering the uncertainty in the input parameters (i.e., rupture velocity, seismic velocity, rock strength, principal stresses, and pore pressure) required for the modeling (Paul et al. 2009). While estimating the permeability for the DZ from these 20 models, we use the value for m=20 that gives the best history match with the mean model. Those 20 equiprobable models show approximately 20 to 30 psi of uncertainty range in the BHP response from injectors and producers. In Well CSI3, which is a gas injector, the uncertainty range from 20 simulations is approximately 30 psi **(Fig. 15a).**

The simulation response of the cumulative water production from all 20 equiprobable models has a better match than the base model. As shown in Fig. 15b, the uncertainty range from different models is approximately 100,000 bbl. These models do not include the uncertainty owing to the aquifer size.

Uncertainty Caused by Methods of Anisotropy Distribution in the Simulation Model. The fault-adjacent gridblocks that exhibit the effect of fault DZs are nonorthogonal and truncated in shape. Therefore, the full permeability tensor is the ideal method to distribute anisotropy in these gridblocks of the simulation model. However, because of simulator limitations, we used the vector projection technique (Eq. 4), which is the arithmetic-average approximation between the matrix permeability and the DZ permeability in the x- and y-direction in a gridblock. DZ permeabilities in the x- and y-direction are estimated using the magnitude of the dot product of full permeability tensor (k) and normal vector (ν) of the grid faces (Eq. 5). This dot-product technique can be used in more general cases, where fault and grid axes are not parallel to each other.

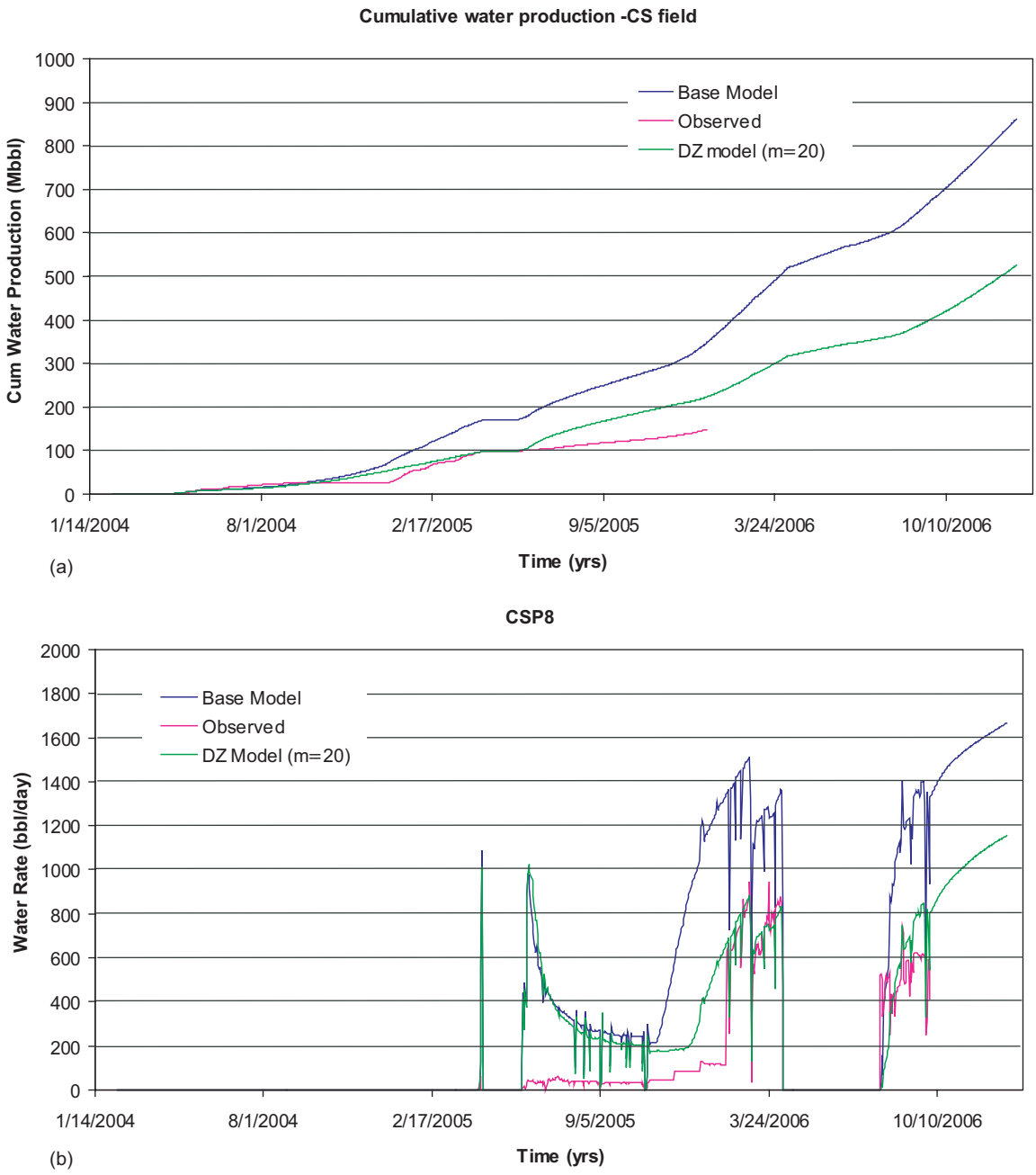

Fig. 14—(a) History matching of the cumulative water production from the field indicates a significant improvement using the DZ model compared with the base model. (b) Water production from Well CSP8 predicted by the DZ model has a better match with the observed production, but it overestimates water production in the earlier period.

$$|k\cdot\nu|_x = (k_h)\sqrt{\left[N^2\cos^2(\omega)+\sin^2(\omega)\right]}, \quad \ldots\ldots\ldots\ldots\ldots\ldots (5a)$$

$$|k\cdot\nu|_y = (k_h)\sqrt{\left[N^2\sin^2(\omega)+\cos^2(\omega)\right]}, \quad \ldots\ldots\ldots\ldots\ldots\ldots (5b)$$

where k_h is the horizontal permeability of the gridblock in the base model, ω is the angle of fault from the x-direction, and N is the fault-parallel permeability multiplier to k_h in the DZ.

The vector projection method is easy to implement, and it gives reasonable results. However, it may overestimate the permeability in either the y- or x-direction for fault orientations with a low angle from x- or y-axis, respectively. This occurs because in these orientations, gridblock permeabilities in the y- and x-direction are close to the harmonic average of the DZ permeability in the respective directions and the gridblock permeability. The error caused by this effect depends on the size of the fault-adjacent gridblocks and orientations of the faults. Larger grid cells tend to show larger error. However, the error is always restricted within a limited zone of the simulation grid, and overall impact on simulation response should be small. This is because in the directions perpendicular to the fault strike, the DZ effect is implemented only in fault-adjacent gridblocks, and the next blocks in those directions are unchanged. We compare the results of Eq. 4 with another anisotropy-distribution method that is similar to Eq. 4, but in this method we do not change the permeability values caused by the DZ in the y- or x-direction for fault orientations 0–20° from the x- or y-axis, respectively, which serves to minimize the error using Eq. 4.

The maximum difference in BHP is approximately 15 psi for producers and approximately 30 psi for the injector **(Fig. 16a).** A difference of approximately 50,000 bbl in cumulative water production (Fig. 16b) is observed at the end of 2 years of production from both the models. The narrow difference in responses (BHP and cumulative water production) from both methods indicates a

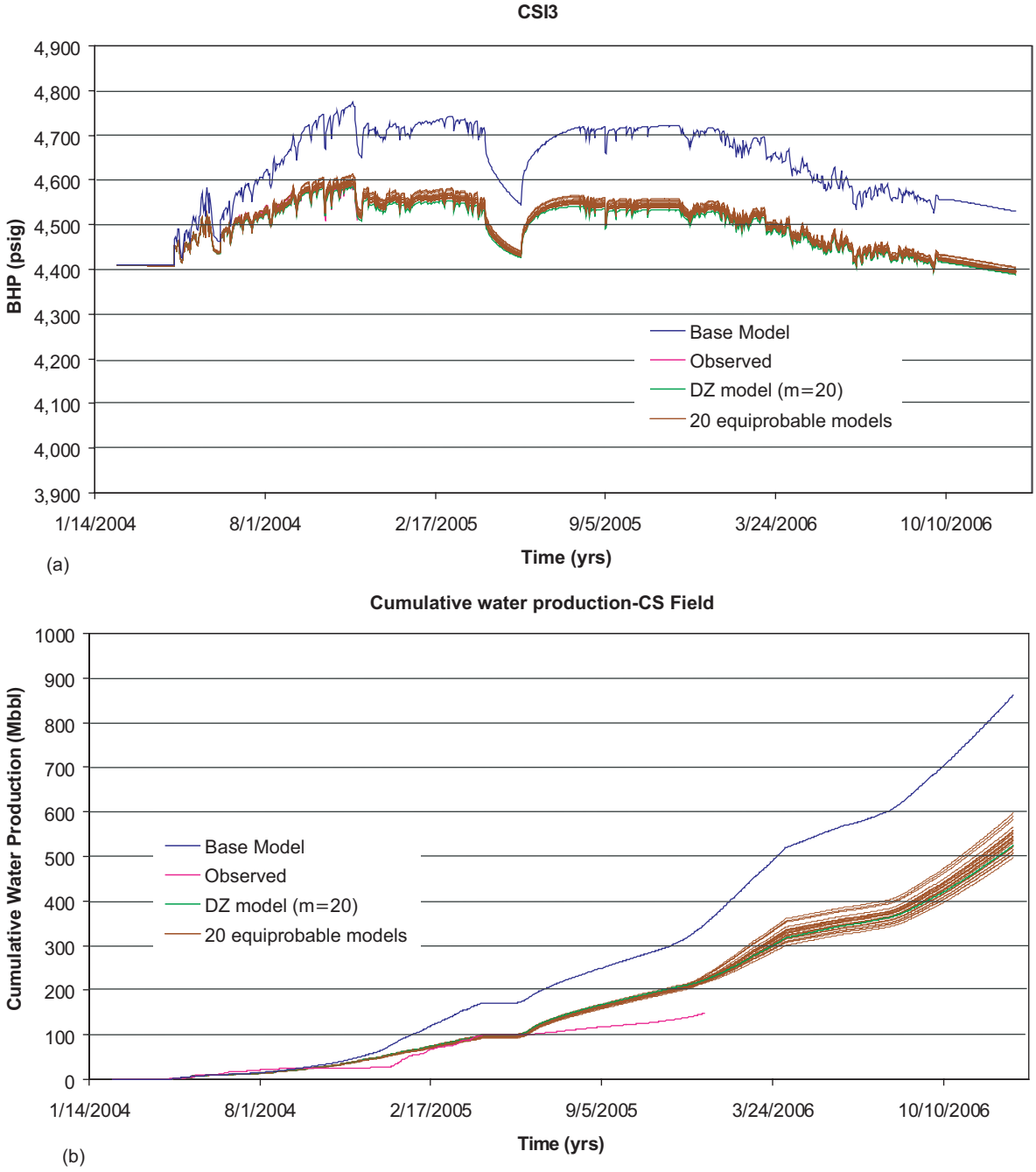

Fig. 15—(a) Simulation responses from the 20 equiprobable models with DZs indicate an uncertainty of approximately 30 psi in the BHP response of Well CSI3. (b) Cumulative water production from the 20 equiprobable DZ models indicates an uncertainty range of approximately 100,000 bbl after 3 years of production. The DZ concept shows a significant improvement in the base model but also shows an increasing range of uncertainty from simulation response with production time.

minimal effect of the error in Eq. 4, discussed in the preceding paragraph. Eq. 5 may give a more accurate result if fault and grid axes are not aligned. In this study, both methods show a good improvement from the base model, verifying the effect of DZs in reservoir-fluid-production behavior.

Uncertainty Because of the Fracture Density of the DZ. In the preceding studies, we used the value of m=20 to represent fracture density, which is equivalent to average fracture density of approximately 2 fractures/m for a 360×380 m gridblock with a DZ approximately 60 m wide. To capture a realistic uncertainty range in the simulation response because of different average fracture density in the DZ, we show two additional cases, m=10 and m=30, which are equivalent to an average fracture density range of approximately 1.2 and 2.5 fractures/m, respectively, for the same gridblock and DZ dimensions. We observe the maximum difference to be approximately 30 psi for producers and approximately 60 psi for the injector **(Fig. 17a).** Cumulative water production from these cases indicate a maximum uncertainty range of approximately 100 Mbbl (Fig. 17b) after a production of 2 years from the reservoir. In all cases, we see a good improvement from the base model, verifying the effect of DZs in reservoir fluid production behavior.

This uncertainty analysis demonstrates the uncertainty range in DZ modeling and its implementation in the simulation model. Although 20 equiprobable models is an insufficient number to give a realistic uncertainty range, it does show the process of capturing the uncertainty trend in the DZ implementation process. All

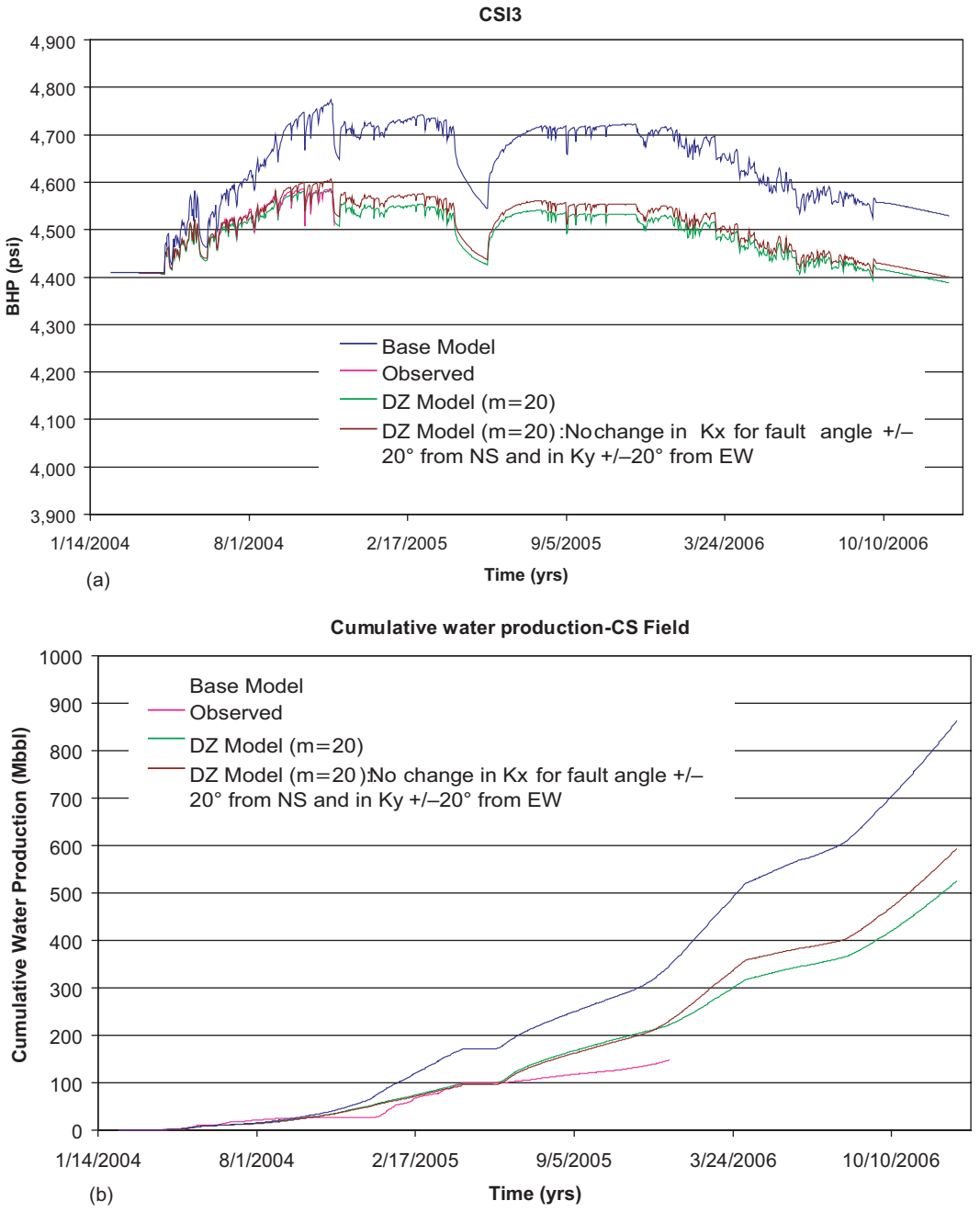

Fig. 16—(a) Simulation responses from both anisotropy-distribution methods indicate an uncertainty of approximately 30 psi in the BHP response of Well CSI3. (b) Simulation response from both anisotropy-distribution methods indicates a difference of approximately 50,000 bbl in cumulative water production from the field after a production of 2 years. Both methods show a good improvement from the base model.

the models show significant improvement in history matching in comparison to the base simulation model, verifying the effect of the DZ in the reservoir fluid-flow behavior.

Conclusions

This paper discusses a method to incorporate fault DZs into a reservoir-simulation model. A DFN study defines the permeability anisotropy caused by DZs, which suggests increased permeability along the strike of the fault and in the vertical direction, but a negligible effect perpendicular to the fault. We captured the effect of DZs in the simulation model by implementing the effects of width, anisotropy, and fracture density of the DZs. The uncertainty analysis using multiple equiprobable DZ models shows a technique to capture the uncertainty related to the DZ modeling and implementation. Also, we found that the DFN analysis with well-scale information and reservoir-scale history matching provide a consistent result of the effect of DZs associated with the reservoir-scale faults.

We successfully demonstrated a workflow to implement DZs in reservoir-simulation models that predict production behavior better. This study includes details to routinely incorporate the method for reservoir studies in the oil and gas industry. However, it is important to understand that the suggested workflow is not designed to model fine-scale details of the DZs in the reservoir-simulation model. Rather, it shows a conceptual and quantitative understanding of the highly permeable zones associated with the reservoir-scale faults, which can potentially provide pathways for reservoir fluids. Also, in addition to DZs, quantifying the uncertainties related to the aquifer size and localized heterogeneities may give a better understanding of the reservoir-pressure behavior with time and create additional confidence in the reservoir model.

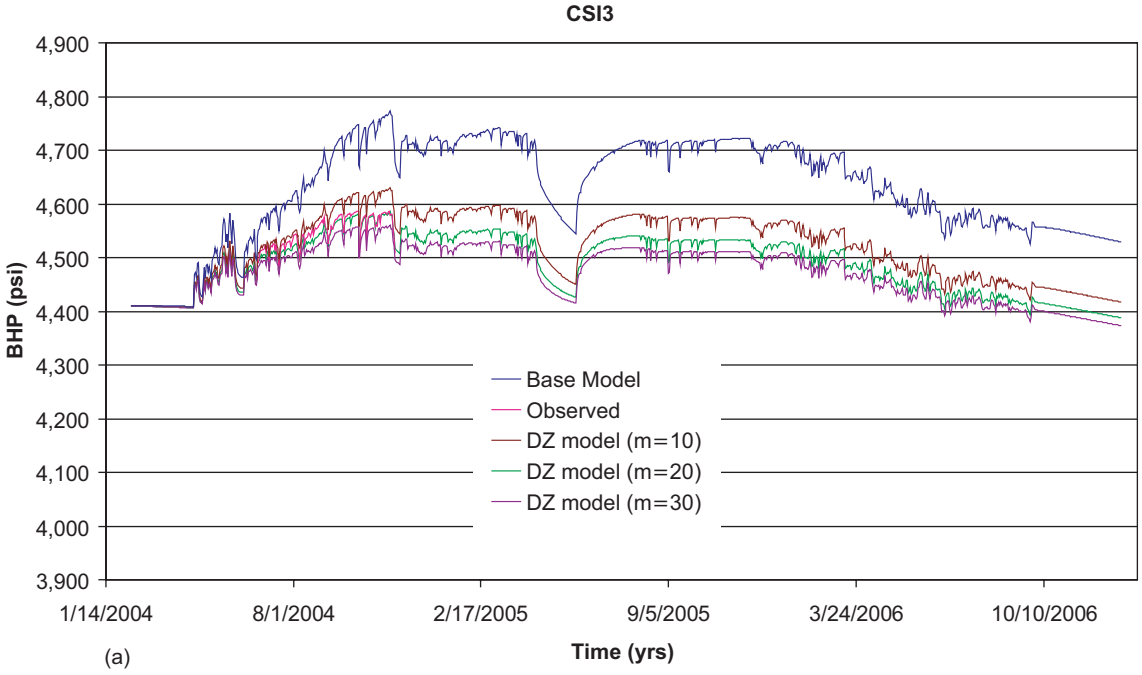

(a)

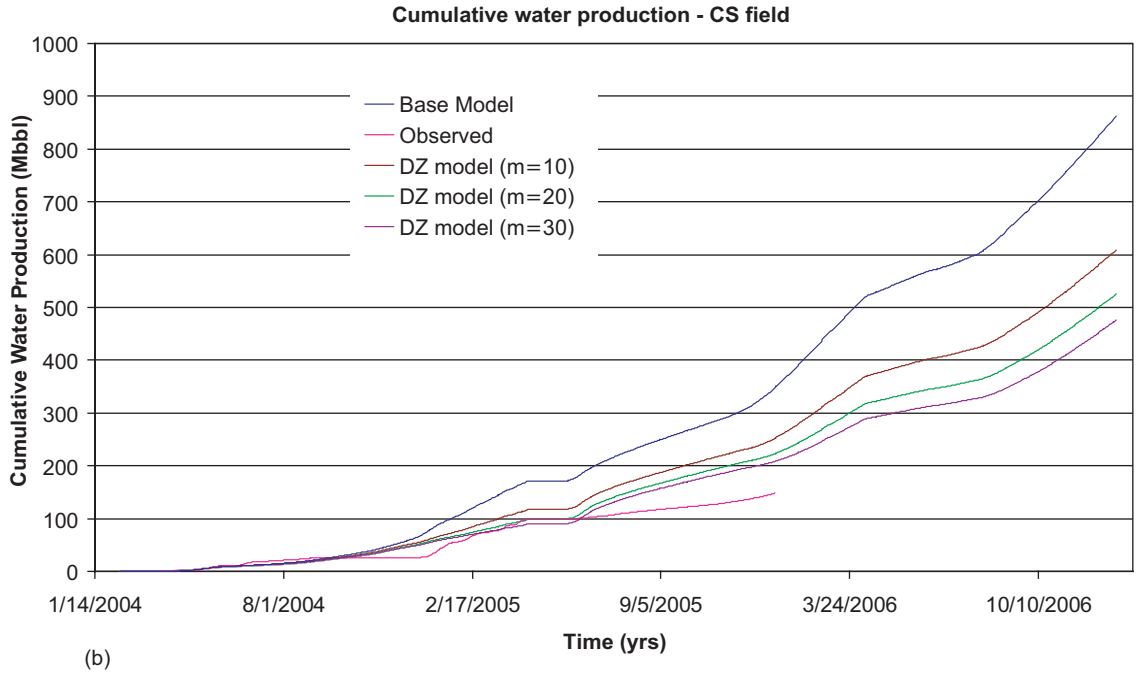

(b)

Fig. 17—(a) Simulation responses for cases of *m* equal to 10, 20, and 30 indicate an uncertainty of approximately 60 psi in the BHP response of Well CSI3. (b) Simulation responses for cases of *m* equal to 10, 20, and 30 indicate an uncertainty of approximately 100,000 bbl in cumulative water production from the field after 2 years of production. All three methods show a better history match than the base model, showing the effect of a DZ.

Nomenclature

a, b = coefficients of permeability/porosity relationship
c = coefficient of vertical- and horizontal-permeability relationship
k = permeability
k^* = upscaled permeability
k_1 = fault-parallel permeability
k_2 = fault-perpendicular permeability
k_h = horizontal permeability
k_m = matrix permeability
k_v = vertical permeability
m = fracture-density factor of DZ in horizontal directions
N = fault-parallel permeability multiplier to k_h in the DZ
S_{wi} = initial water saturation
ν = normal vector
ΔP = pressure difference
ϕ = porosity
ω = angle of the fault from x-direction

Acknowledgments

We thank ConocoPhillips for providing the data for this investigation and the base simulation model, and giving us permission to publish this paper. We also want to thank the Stanford Rock Physics and Borehole Geophysics consortium for funding this project. We want to thank Louis Durlofsky from the Department of Energy Resource Engineering, Stanford University, for his valuable guidance

throughout this research. In addition, we want to acknowledge Mohammad Karimi-Fard and Bin Gong from the Department of Energy Resource Engineering, Stanford University, for their useful advice during various parts of the project.

References

Aarnes, J.E., Lie, K.-A., Kippe, V., and Krogstad, S. 2009. Multiscale Methods for Subsurface Flow. In *Multiscale Modeling and Simulation in Science*, ed. B. Engquist, P. Lötstedt, and O. Runborg, No. 66, 3–48. Berlin: Lecture Notes in Computational Science and Engineering, Springer-Verlag.

Ahmadov, R., Aydin, A., Karimi-Fard, M., and Durlofsky, L.J. 2007. Permeability upscaling of fault zones in the Aztec Sandstone, Valley of Fire State Park, Nevada, with a focus on slip surfaces and slip bands. *Hydrogeology* **15** (7): 1239–1250. doi: 10.1007/s10040-007-0180-2.

Brown, S.R. and Bruhn, R.L. 1998. Fluid permeability of deformable fracture networks. *J. of Geophysical Research* **103** (B2): 2489–2500. doi: 10.1029/97JB03113.

Ciment, M. and Sweet, R.A. 1973. Mesh refinements for parabolic equations. *J. of Computation Physics* **12** (4): 513–525. doi: 10.1016/0021-9991(73)90102-2.

Corbett, P.W.M., Ringrose, P.S., Jensen, J.L., and Sorbie, K.S. 1992. Laminated Clastic Reservoirs: The interplay of Capillary pressure and Sedimentary Architecture. Paper SPE 24699 presented at the SPE Annual Technical Conference and Exhibition, Washington, DC, 4–7 October. doi: 10.2118/24699-MS.

Durlofsky, L.J. 2003. Upscaling of Geocellular Models for Reservoir Flow Simulation: A Review of Recent Progress. Presented at the International Forum on Reservoir Simulation, Bühl/Baden-Baden, Germany, 23–27 June.

Flodin, E.A., Aydin, A., Durlofsky, L.J., and Yeten, B. 2001. Representation of fault zone permeability in reservoir flow models. Paper SPE 71617 presented at the SPE Annual Technical Conference and Exhibition, New Orleans, 30 September–3 October. doi: 10.2118/71617-MS.

Freund, L.B. 1979. The Mechanics of Dynamic Shear Crack Propagation. *J. of Geophysical Research* **84** (B5): 2199–2209. doi: 10.1029/JB084iB05p02199.

Geiger, S., Huangfu, Q., Reid, A.F., Matthai, S., Coumou, D., Belayneh, M., Fricke, C., and Schmid, K. 2009. Massively Parallel Sector Scale Discrete Fracture and Matrix Simulations. Paper SPE 118924 presented at the SPE Reservoir Simulation Symposium, The Woodlands, Texas, USA, 2–4 February. doi: 10.2118/118924-MS.

Gong, B., Karimi-Fard, M., and Durlofsky, L.J. 2008. Upscaling Discrete Fracture Characterizations to Dual-Porosity, Dual-Permeability Models for Efficient Simulation of Flow With Strong Gravitational Effects. *SPE J.* **13** (1): 58–67. SPE-102491-PA. doi: 10.2118/102491-PA.

Jourde, H., Flodin, E.A., Aydin, A., Durlofsky, L.J., and Wen, X. 2002. Computing Permeability of Fault Zones in Eolian Sandstone from Outcrop Measurements. *AAPG Bulletin* **86** (7): 1187–1200. doi: 10.1306/61EEDC4C-173E-11D7-8645000102C1865D.

Karimi-Fard, M., Durlofsky, L.J., and Aziz, K. 2004. An Efficient Discrete-Fracture Model Applicable for General-Purpose Reservoir Simulators. *SPE J.* **9** (2): 227–236. SPE-88812-PA. doi: 10.2118/88812-PA.

Koutsabeloulis, N.C., Heffer, K.J., and Wong, S. 1994. Numerical geomechanics in reservoir engineering. In *Computer Methods and Advances in Geomechanics*, ed. H. Siriwardane and M. Zaman, 2097–2104. Rotterdam, The Netherlands: A.A. Balkema.

Lim, K.-T., Hui, M.-H., and Mallison, B. 2009. A Next-Generation Reservoir Simulator as an Enabling Technology for a Complex Discrete Fracture Modeling Workflow. Paper SPE 124980 presented at the SPE Annual Technical Conference and Exhibition, New Orleans, 4–7 October. doi: 10.2118/124980-MS.

Luthi, S.M. and Souhaité, P. 1990. Fracture apertures from electrical borehole scans. *Geophysics* **55** (7): 821–833. doi: 10.1190/1.1442896.

Madariaga, R. 1976. Dynamics of an expanding circular fault. *Bulletin of the Seismological Society of America* **66** (3): 639–666.

Mlacnik, M.J. and Heinemann, Z.E. 2003. Using Well Windows in Full Field Reservoir Simulation. *SPE Res Eval & Eng* **6** (4): 275–285. SPE-85709-PA. doi: 10.2118/85709-PA.

Nacul, E.C. 1991. Use of Domain Decomposition and Local Grid Refinement in Reservoir Simulation. PhD dissertation, Department of Petroleum Engineering, Stanford University, Stanford, California, USA (March 1991).

Pande, G.N. 1980. Numerical simulation of rock behavior: problems and possibilities. *Numerical Methods in Geomechanics* 4: 1341–1356.

Paul, P., Zoback, M., and Hennings, P. 2009. Fluid Flow in a Fractured Reservoir Using a Geomechanically Constrained Fault-Zone-Damage Model for Reservoir Simulation. *SPE Res Eval & Eng* **12** (4): 562–575. SPE-110542-PA. doi: 10.2118/110542-PA.

Pedrosa, O.A. and Aziz, K. 1986. Use of a Hybrid Grid in Reservoir Simulation. *SPE Res Eng* **1** (6): 611–621; *Trans.*, AIME, **281.** SPE-13507-PA. doi: 10.2118/13507-PA.

Pickup, G.E. and Stephen, K.D. 2000. An assessment of steady-state scale-up for small-scale geological models. *Petroleum Geoscience* **6** (3): 203–210. doi: 10.1144/petgeo.6.3.203.

Pickup, G.E., Ringrose, P.S., and Sharif, A. 2000. Steady-State Upscaling: From Lamina-Scale to Full-Field Model. *SPE J.* **5** (2): 208–217. SPE-62811-PA. doi: 10.2118/62811-PA.

Rasaei, M.R. and Sahimi, M. 2009. Upscaling of the Geological Models of Large-Scale Porous Media Using Multiresolution Wavelet Transformations. *J. Heat Transfer* **131** (10): 101007–101019. doi: 10.1115/1.3167544.

Ringrose, P.S., Sorbie, K.S., Corbett, P.W.M., and Jensen, J.L. 1993. Immiscible flow behavior in laminated and cross-bedded sandstone. *J. Pet. Sci. Eng.* **9** (2): 103–124. doi: 10.1016/0920-4105(93)90071-L.

Rodriguez, J.F., Bombardelli, F.A., Garcia, M.H., Fronthingham, K.M., Rhoads, B.L., and Abad, J.D. 2004. High-resolution Numerical Simulation of Flow Through a Highly Sinuous River Reach. *Water Resources Management* **18** (3): 177–199. doi: 10.1023/B:WARM.0000043137.52125.a0.

Søriede, I. and Whitson, C.H. 1992. Peng Robinson predictions for hydrocarbons, CO_2, N_2 and H_2S with pure water and NaCl-Brines. *Fluid Phase Equilibria* **77** (15): 217–240. doi: 10.1016/0378-3812(92)85105-H.

Verma, S.K. and Aziz, K. 1997. A Control Volume Scheme for Flexible Grids In Reservoir Simulation. Paper SPE 37999 presented at the SPE Reservoir Simulation Symposium, Dallas, 8–11 June. doi: 10.2118/37999-MS.

SI Metric Conversion Factors

ft × 3.048*	E–01 = m
md × 10^{-15}	E–02 = m^2
psi × 6.894 757	E–03 = MPa

* Conversion factor is exact.

Pijush Paul works in the structure and geomechanics team of ConocoPhillips Subsurface Technology Group in Houston. E-mail: pijush.k.paul@conocophillips.com. He leads the team's computational geomechanics program. Paul's other projects focus on providing geomechanical models of reservoirs for drilling, completion and production optimization. He holds a PhD degree in geomechanics and MS degree in petroleum engineering from Stanford University, an MTech degree in applied geophysics from the Indian Institute of Technology, and a BS(Hons) degree in geology and physics from St. Xavier College, India. **Mark Zoback** has been a professor of geophysics at Stanford University since 1984. His principal research interests are related to the forces that act within the Earth's crust and their influence on processes related to plate tectonics, earthquakes, and oil and gas reservoirs. Zoback is the author of the technical reference book *Reservoir Geomechanics*, published in 2007 by Cambridge University Press. **Peter Hennings** is the manager of the structure and geomechanics group in ConocoPhillips Technology and is active in its global technical service, research, and knowledge sharing missions. He is an adjunct professor of geology at the University of Wyoming and serves on the UW enhanced oil recovery advisory board. Hennings holds a PhD degree in structural geology from the University of Texas and BS and MS degrees in geology from Texas A&M University. He is an honorary fellow of the Geological Society of America and is an American Association of Petroleum Geologists Distinguished Lecturer. Hennings' geoscience specialties include seismic interpretation, fractured reservoir analysis, and geoscience instruction.